Predicted Performance of a Tangential Viewing Hard X-Ray Camera for the DIII-D High Field Side Lower Hybrid Current Drive Experiment

Grant Rutherford,[1, a)] Andrew H. Seltzman,[1] and Stephen J. Wukitch[1]
Plasma Science and Fusion Center, Massachusetts Institute of Technology, Cambridge, Massachusetts 02142, USA

(Dated: May 2022)

High field side (HFS) launch of lower hybrid current drive (LHCD) has improved accessibility and penetration over low field side launch on DIII-D. Simulations predict single pass absorption under a wide range of plasma conditions. Hard x-ray (HXR) measurement of LHCD generated fast electron bremsstrahlung (50-250 keV) will validate wave propagation and absorption. Emissivity profiles are recovered from 1 dimensional inversion of HXR brightness to determine LH damping location, fast electron slowing down time, and some indication of the fast electron energy. The camera will be implemented by populating 32 tangential sightlines of the existing Gamma Ray Imager with Kromek SPEAR^{TM} Cadmium Zinc Telluride (CZT) detectors sensitive to 10-1000 keV photons with 10 keV energy resolution. Expected count rates allow for <0.5 ms time resolution. Pulses are processed using 50 ns shaping time Cremat CR-200 gaussian shaping modules and are digitized by 25 MHz D-TACQ ACQ216 digitizers. Performance of the HXR camera is evaluated by comparing predicted fast electron density profiles and inverted synthetic brightnesses obtained from the ray-tracing/Fokker-Plank codes GENRAY/CQL3D. Inversions closely matched predicted fast electron profiles for a range of experimental parameters.

I. INTRODUCTION

High field side (HFS) launch of lower hybrid current drive (LHCD) has improved accessibility and penetration over low field side launch.[1] The first test of this technology will occur on DIII-D with the installation of a new launcher,[2] where single pass absorption is predicted under a wide range of plasma conditions.[3] Wave propagation and absorption will be validated with a hard x-ray (HXR) camera imaging 50-250 keV photons emitted via bremsstrahlung radiation by LHCD-generated fast electrons. The measured brightness is inverted in one dimension using an algorithm detailed in Section II. The resulting HXR emissivity vs ρ profile is proportional to the fast electron density (denoted $n_{e,\,fast}$) profile and thus indicates where the LH waves damp. Hard X-ray cameras have been installed as part of the LH systems on Alcator C-mod[4], Tore Supra[5], PBX-M[6], and other devices.

A collimated pinhole HXR camera will be implemented on DIII-D by populating 32 tangential sightlines of the existing Gamma Ray Imager[7] (GRI) with Kromek SPEAR$^{™}$ CZT diodes. A cross section of the GRI with its BGO diodes installed is shown in Fig 1. Tangential sightlines preferentially measure HXR emission from forward-moving fast electrons, which improves localization of the LH damping location. In the case of poloidal sightlines, a significant portion of the measured brightness may stem from pitch-angle scattered electrons,[8] which have undergone many collisions and hence degrade localization of the damping location. A projection of our chosen sightlines (which are stacked in vertical columns) onto the toroidal midplane is shown in Fig. 2. Fig 3 gives the poloidal projection of the sightlines where they are most tangential to the magnetic field together with the predicted count rates of the channels and the LH rays for discharge 147364 with $n_{\parallel} = -2.7$.

Filtering by a 6.35 mm (1/4") sapphire vacuum window and a 1.5875 mm (1/16") 316L stainless steel plate (for protection of the window from ECH) attenuates the dominant low-energy thermal background. The attenuation curves are provided in Fig 4. Detector pulses are shaped using 50 ns Cremat CR-200 gaussian amplifiers before digitization by D-TACQ ACQ216 digitizers operating at 25 MHz.

Digitization of the signal allows for flexible time and energy binning in post-processing. With the count rates predicted for our target case, discharge 147634 with $n_{\parallel} = -2.7$, a time resolution of 0.5 ms is expected while satisfying $\frac{\sqrt{(dN/dt)\Delta t}}{(dN/dt)\Delta t} < 10\%$, where dN/dt is the number of counts measured per second and Δt is the time resolution. 10 keV energy resolution and a minimum resolvable distance between separate peaks of at most 0.2ρ are also expected.

II. INVERSION ALGORITHM

To simplify our inversion problem to one dimension, we assumed that $n_{e,\,fast}$ is constant along flux surfaces, greatly relaxing requirements on the number and views of the sightlines. Our inversion algorithm is an adaptation of the modified Abel inversion presented in [9] paired with minimum Fisher information (MFI) regularization.

The traditional Abel inversion discretizes space in terms of ρ, so the line-integrated emissivity (i.e. the brightness) is given by $\vec{B} = \boldsymbol{L}\vec{E}$, where $\vec{B}$ is the mea-

[a)]The author to whom correspondence may be addressed: grantr@mit.edu

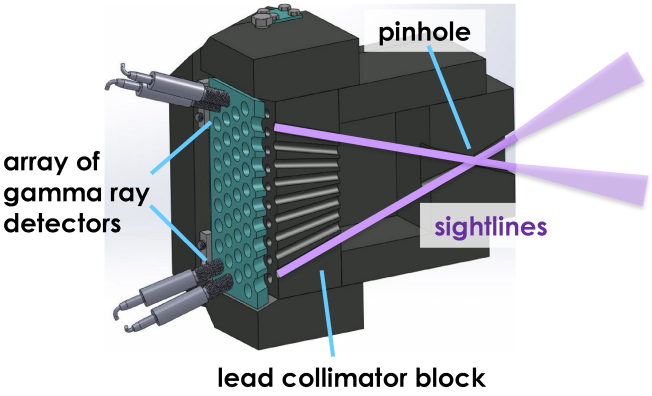

FIG. 1: Cross section of the Gamma Ray Imager (GRI) with its typical BGO detectors installed. Reproduced from A. Lvovskiy, C. Paz-Soldan, N. Eidietis et al., Upgrades to the Gamma Ray Imager on DIII-D Enabling Access to High Flux Hard X-Ray Measurements During the Runaway Electron Plateau Phase, Review of Scientific Instruments, these Proceedings, 2022, with the permission of AIP Publishing.

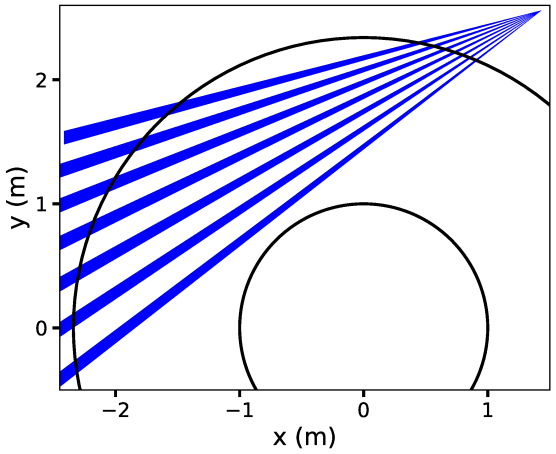

FIG. 2: Projection of our chosen GRI sightlines, which are stacked vertically, onto DIII-D's toroidal midplane.

sured brightnesses, $\boldsymbol{L}$ is the length matrix describing the length of each sightline in each ρ bin, and $\vec{E}$ is the discretized emissivity profile. Multiplying both sides by $\boldsymbol{L}^{-1}$ produces $\vec{E} = \boldsymbol{L}^{-1}\vec{B}$.

The modification given by [9] accounts for the anistropy of bremsstrahlung emission in this energy range[10] by multiplying each element of $\boldsymbol{L}$ by a $\cos^n(\theta)$ term, where n is some free parameter and θ is the angle between the sightline and the local magnetic field. n has only a minor effect on the inversion accuracy for our chosen sightlines. If we rotate the sightlines to become more poloidally-viewing, n becomes an important parameter for achieving good inversions. Tangential sightlines

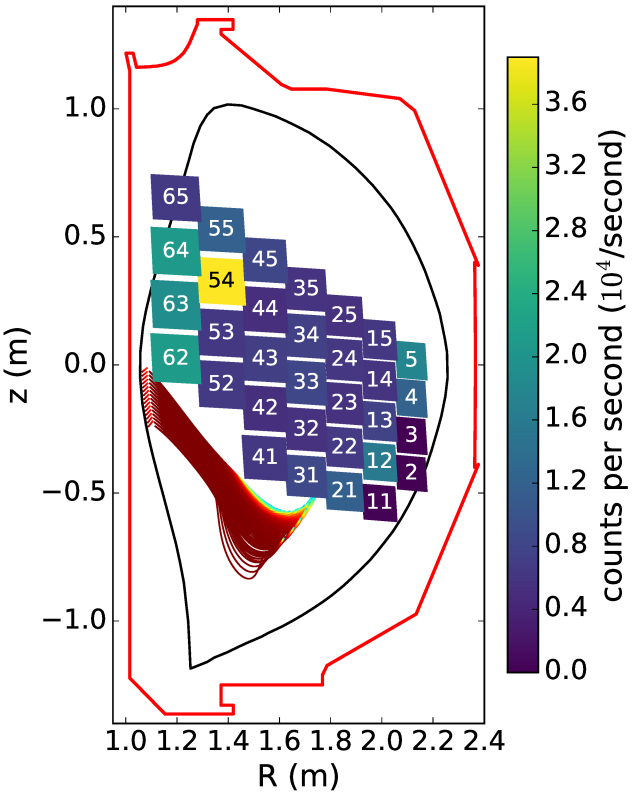

FIG. 3: Poloidal projection of the sightlines where they are most tangent to the magnetic field together with the predicted count rates and LH rays for discharge 147364 with $n_{||} = -2.7$.

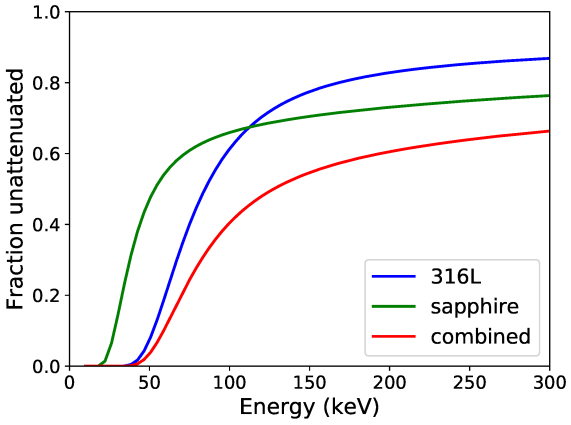

FIG. 4: Fraction of photons passing through the sapphire window and 316L stainless steel plate separating the GRI from the plasma.

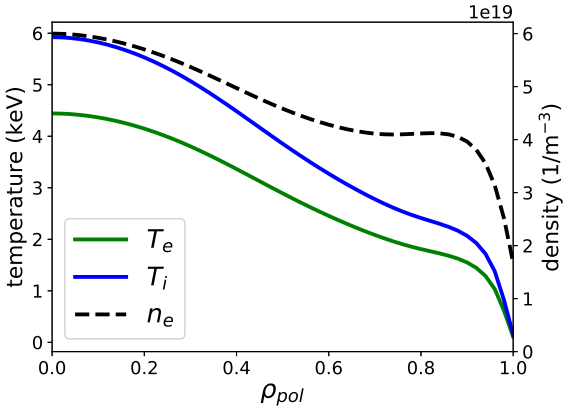

FIG. 5: The electron temperature, ion temperature, and total electron density for discharge 147634

therefore further simplify analysis.

Due to the limited number of sightlines, minimum Fisher information (MFI) regularization, which has the effect of enforcing smoothness in low emissivity regions but relaxing this constraint in high emissivity regions (i.e. where there is a peak), is employed to obtain physically-reasonable inversions.[11] Implementation of MFI regularization and other improvements over the basic Abel inversion are described in [12].

III. RESULTS

Performance of the inversion algorithm is evaluated with the ray-tracing/Fokker-Plank codes GENRAY[13]/CQL3D[14] to obtain a synthetic brightness (which accounts for the anisotropy of emission) and a predicted fast electron density profile for a variety of experimental parameters. The synthetic brightness for energies between 50 and 250 keV is then inverted together, whereas different energy bins may be inverted separately during operation of the camera, and the resulting emissivity should match $n_{e,\,fast}$ up to a scaling factor. Unless stated otherwise, all simulations assumed 1 MW of LH power (.96 MW in the forward lobe, .04 MW in the reverse lobe) and a flat $Z_{\text{eff}} = 2$ profile.

The high q_{min} discharge 147634 (see Fig 5 for the relevant profiles) was used as a target discharge due to excellent penetration and absorption characteristics.[3] The inverted brightnesses given by simulations of this discharge with $n_\parallel$s of $-2.3, -2.7$, and -3.1 are compared against the corresponding $n_{e,\,fast}$ profiles in Fig 6 (a), (b), and (c), respectively. We define a fast electron to have an energy of 50 keV or above. Also plotted in Fig 5 are the RF deposition profiles. In all cases, the non-thermal emissivity peak (i.e. the off axis peak) is accurately matched by the inversion. The thermal emissivity peak (i.e. the core emissivity), however, is matched with varying degrees of success, with the $n_\parallel = -3.1$ inversion nearly predicting the correct behavior, and the $n_\parallel = -2.3$ inversion predicting zero core emissivity. Given that our focus is the non-thermal peak, these inversions are more than sufficient to achieve our objectives.

Looking at the RF deposition profiles of Fig 6, it is interesting to note that the deposition and $n_{e,\,fast}$ peaks are nearly co-located in the $n_\parallel = -2.3$ and -3.1 cases, but less so in the $n_\parallel = -2.7$ case. We are therefore unable to assume that $n_{e,\,fast}$ peak directly matches the damping location of the LH waves. We will thus instead need to match the $n_{e,\,fast}$ profile to a model to estimate the location of the deposition peak.

To evaluate the inversion's sensitivity to the thermal background, simulations were completed with reduced LH power. Shown in Fig 7 is the resulting inversion for 0.5 MW, where the nonthermal peak is fit well. Given that the launcher anticipated to inject 0.9 MW for $n_\parallel = -2.7$,[15] highly accurate inversions are expected to be possible. Below 0.5 MW, the width of the nonthermal peak is slightly overestimated, and its amplitude is somewhat underestimated.

Inversions with two separate but simultaneous $n_\parallel$s evaluate the minimum resolvable distance between peaks in anticipation of a future second launcher installation. Waves are launched with $n_\parallel = -2.3$ (0.33 MW) and -2.7 (0.66 MW) in Fig 8 (a) and with $n_\parallel = -2.3$ (0.33 MW) and -3.1 (0.66 MW) in Fig 8 (b) for discharge 147634. The reconstructed non-thermal peaks are distinctly resolved and their locations accurately determined, though some deviation in peak amplitude is present.

The final test of the inversion algorithm was to attempt inversions for additional discharges. The inversions, $n_{e,\,fast}$ profiles, and RF deposition profiles for $n_\parallel = -2.7$ and discharges 144476 (a), 161418 (b), and 172461 (c) are given in Fig 9. 144476 is a 2 T AT discharge, 161418 is a super H-mode, and 180692 is another high q_{min} plasma. These shots were chosen to get a wide range of example $n_{e,\,fast}$ profiles.

The non-thermal 144476 $n_{e,\,fast}$ peak is reconstructed well, however fine detail of the low amplitude peak separation at the plasma edge was lost. The 161418 non-thermal $n_{e,\,fast}$ peak was underestimated but good spatial localization was maintained. Inversion of 60-250 keV photons resulted in an improved fit, though still less accurate than the inversions of Fig 6. The 180692 $n_{e,\,fast}$ profile is reconstructed with a slightly broadened non-thermal peak shifted a small distance towards the edge. Even with the noted discrepancies, these inversions would permit validation of HFS wave physics.

IV. CONCLUSION

Using 32 of the Gamma Ray Imager's tangential sightlines retrofitted with Kromek SPEAR™ CZT diodes, inversions of the measured HXR brightness are predicted to be highly accurate for a variety of expected experi-

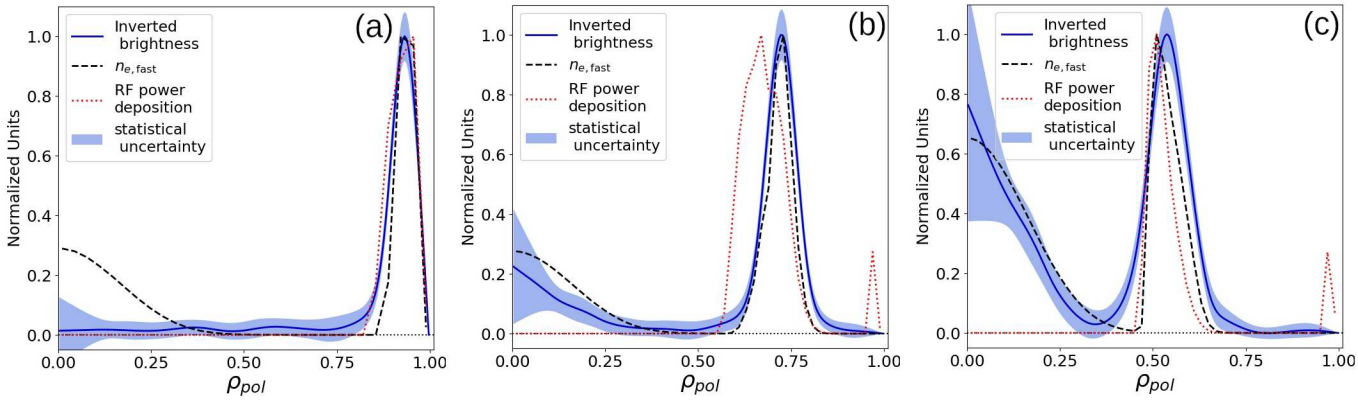

FIG. 6: Inverted synthetic brightness, predicted fast electron density profile, and RF power deposition profile for discharge 147634 with $n_{\|} = -2.3$ (a), -2.7 (b), and -3.1 (c).

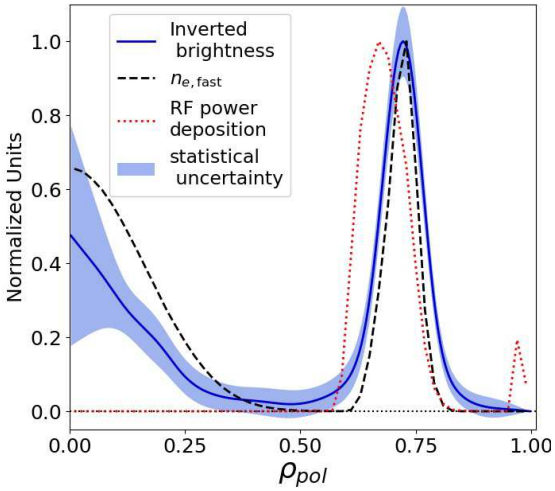

FIG. 7: Inverted synthetic brightness, predicted fast electron density profile, and RF power deposition profile for discharge 147634 with $n_{\|} = -2.7$ and 0.5 MW of LH power

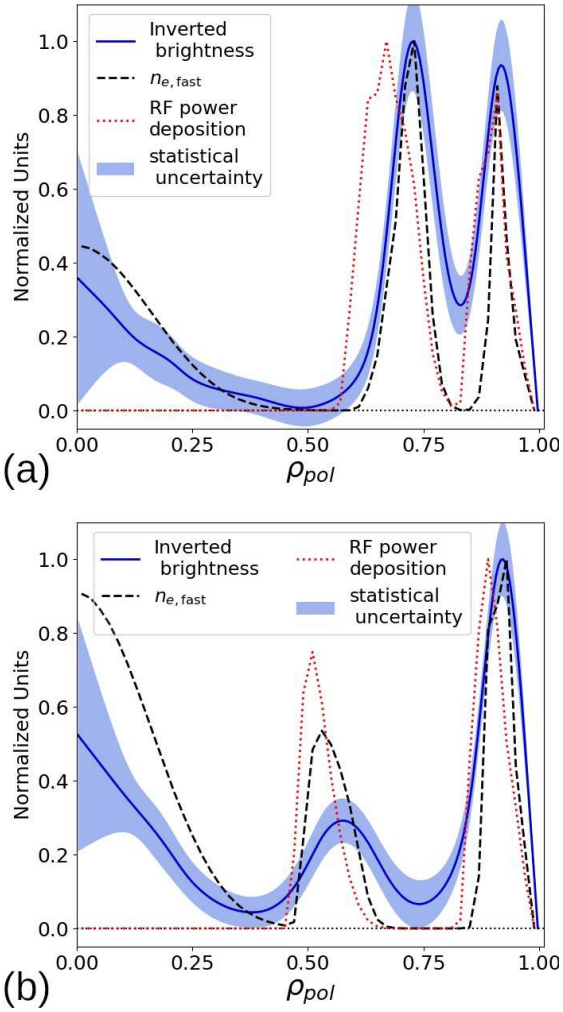

FIG. 8: Inverted synthetic brightness, predicted fast electron density profile, and RF power deposition profile for discharge 147634 with $n_{\|} = -2.3$ and -2.7 (a) and $n_{\|} = -2.3$ and -3.1 (b).

mental conditions. Future work includes calibrating detectors, mounting two detectors temporarily on the GRI to measure the potential effects of neutrons and neutron-induced gammas, and developing related hardware.

ACKNOWLEDGEMENTS

The authors would like to thank Tomáš Odstrčil for adapting his tomography code to suit this diagnostic and Andrey Lvovskiy for sharing his wealth of knowledge on the Gamma Ray Imager. This work is supported by the U.S. Department of Energy, Office of Science, Office of Fusion Energy Sciences, using User Facility DIII-D, under Award Number DE-FC02-04ER54698, US DoE award SC0014264, and by US DoE Contract No. DE-FC02-01ER54648 under a Scientific Discovery through

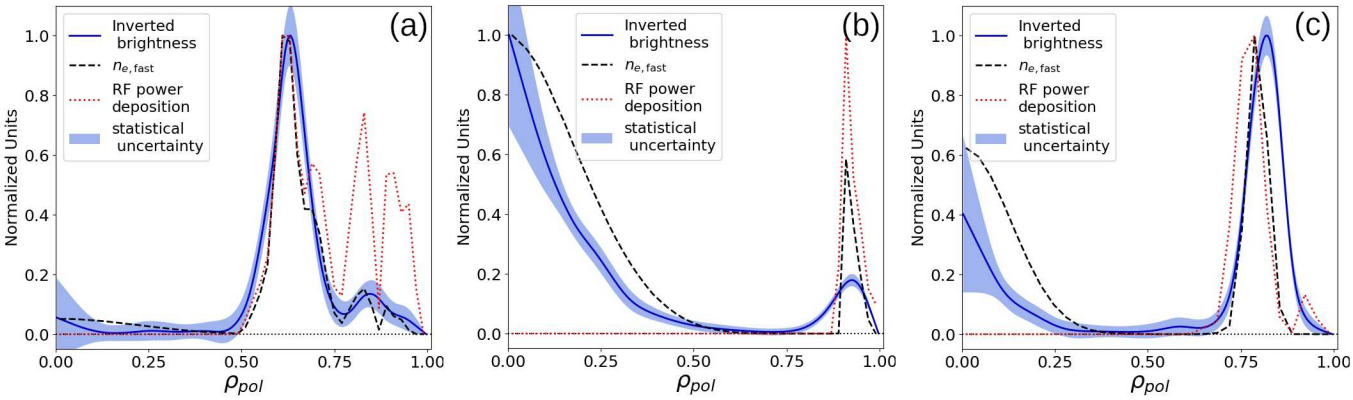

FIG. 9: Inverted synthetic brightness, predicted fast electron density profile, and RF power deposition profile for $n_{\|} = -2.7$ and discharge 144476 (a), 161418 (b), and 180692 (c).

Advanced Computing Initiative.

DATA AVAILABILITY

The GENRAY and CQL3D namelists and any other data used in this work are available from the corresponding author upon request.

[1]P. Bonoli *et al.*, Nuclear Fusion **58**, 126032 (2018).
[2]A. Seltzman, S. Shiraiwa, G. Wallace, and S. Wukitch, Nuclear Fusion **59**, 096003 (2019).
[3]S. J. Wukitch *et al.*, in *European Physical Journal Web of Conferences*, European Physical Journal Web of Conferences, Vol. 157 (2017) p. 02012.
[4]J. Liptac *et al.*, Review of Scientific Instruments **77**, 103504 (2006), https://doi.org/10.1063/1.2214695.
[5]O. Barana *et al.*, in *14th IEEE-NPSS Real Time Conference, 2005.* (2005) pp. 5 pp.–.
[6]S. von Goeler *et al.*, Review of Scientific Instruments **65**, 1621 (1994), https://doi.org/10.1063/1.1144850.
[7]D. C. Pace *et al.*, Review of Scientific Instruments **87**, 043507 (2016), https://doi.org/10.1063/1.4945566.
[8]A. E. W. Schmidt, *Measurements and Modeling of Lower Hybrid Driven Fast Electrons on Alcator C-Mod*, Ph.D. thesis, Massachusetts Institute of Technology (2011).
[9]R. E. Bell, Review of Scientific Instruments **66**, 558 (1995), https://doi.org/10.1063/1.1146350.
[10]S. V. Goeler *et al.*, Nuclear Fusion **25**, 1515 (1985).
[11]M. Anton *et al.*, Plasma Physics and Controlled Fusion **38**, 1849 (1996).
[12]T. Odstrčil *et al.*, Review of Scientific Instruments **87**, 123505 (2016), https://doi.org/10.1063/1.4971367.
[13]A. Smirnov and R. Harvey, Bull. Am. Phys. Soc **40**, 35 (1995).
[14]R. Harvey and M. McCoy, in *Proceedings of the IAEA Technical Committee Meeting on Simulation and Modeling of Thermonuclear Plasmas* (1992) pp. 489–526.
[15]A. Seltzman and S. Wukitch, Fusion Engineering and Design **159**, 111762 (2020).